Energy Storage

WILEY

ENERGY STORAGE

RESEARCH ARTICLE

Effect of Ni Incorporation in $KCoPO_4$ on the Charge Storage Capacity of $KCo_{1-x}Ni_xPO_4$ ($0 \leq x \leq 0.5$) Electrodes for the Fabrication of High-Performing Hybrid Supercapacitors

Krishna Gopal Nigam[1] | Abhijeet Kumar Singh[1] | Soham Mukherjee[1] | Asha Gupta[2] | Preetam Singh[1]

[1]Department of Ceramic Engineering, Indian Institute of Technology (Banaras Hindu University), Varanasi, India | [2]Department of Chemistry, Indian Institute of Technology (Banaras Hindu University), Varanasi, India

Correspondence: Preetam Singh (preetamsingh.cer@itbhu.ac.in; preetamchem@gmail.com)

Received: 20 October 2024 | **Revised:** 26 November 2024 | **Accepted:** 11 December 2024

Funding: This work was supported by the Cellgrid Energy Pvt. Ltd (UID0991).

Keywords: aqueous battery | energy storage | hybrid supercapacitors

ABSTRACT

Fulfilling the increasing energy demands of the world through renewable energy sources requires the utilization of a highly efficient large-scale electrochemical energy storage device. A hybrid supercapacitor (HSC) that consists of a battery-type electrode coupled with a counter-capacitive electrode, while in principle offering supercapacitor-like power, cyclability, and higher energy density, can be a potential device for large-scale energy storage to cater to the energy needs through renewable energy sources. The $KCo_{0.5}Ni_{0.5}PO_4$ electrode demonstrated notably enhanced electrochemical performance, attributed to the synergistic interaction of Co^{2+} and Ni^{2+} ions in a phosphate framework. The incorporation of redox-mediated diffusive charge storage through the incorporation of Ni^{2+} on the Co^{2+} site resulted in a large-scale charge storage capacity, coupled with capacitive-type surface charge storage on the $KCo_{1-x}Ni_xPO_4$ electrodes. The $KCo_{0.5}Ni_{0.5}PO_4$ delivers 173 mAh/g (capacitance: 1038 F/g) at a current density of 0.5 A/g in an aqueous 2 M KOH electrolyte, accompanied by cyclic stability up to 5000 cycles. HSC mode consists of activated carbon as the negative electrode along with $KNi_{0.5}Co_{0.5}PO_4$ as the positive electrode, displaying high energy density and power density of 183.7 Wh/kg and 7952 W/kg, respectively, in 2 M aqueous KOH electrolyte. The superior performance in HSC mode makes $KCo_{0.5}Ni_{0.5}PO_4$ a potential positive electrode for the development of high-performing HSCs.

1 | Introduction

Increasing energy demand to sustain the growth and development of the world is met by burning fossil fuels, resulting in global warming. To meet global energy needs, harnessing energy from renewable energy sources such as solar, wind, and tides can be a prominent solution [1–3]. However, power produced through renewable sources faces fluctuations due to dependency on weather conditions. To effectively overcome these fluctuations and supply stable power through renewable sources such as solar, wind, or tidal, large-scale electrochemical energy conversion and storage devices are required [3–8]. Batteries and supercapacitors have recently gained more attention due to their superior performance in terms of excellent efficiency, cyclic stability, energy density, and fast charging/discharging at high current rates. Batteries have high energy density because ions enable redox reactions in bulk electrode materials, which are diffusion controlled. On the contrary, supercapacitors store charge by the adsorption of electrolyte ions onto the surface of electrode materials [5]. Notably, the low power density of the batteries due to the sluggish faradic charge storage mechanism and the low energy density of supercapacitors due to the double-layer charge storage on the electrode surface have made researchers deliberately contemplate hybrid energy storage devices [5–7]. A hybrid supercapacitor (HSC) is a relatively new device that consists of a battery-type electrode coupled with a counter-capacitive electrode, while in principle offering supercapacitor-like power, cyclability, and higher energy density [9].

The selection of electrode material is a crucial step toward creating effective and reliable HSCs. Carbon-based materials, such as activated carbon, can be used as negative electrodes for delivering high power density with long-lasting cycles without any constraints [3–10]. Moreover, the positive electrode must be a battery-type material, capable of delivering high energy density with minimal loss of capacity over cycles. However, oxide-based electrodes show slow kinetics with low cyclic stability, which ultimately limits the attainment of higher power density and stable life cycles [11, 12]. Polyanion frameworks indicate a class of materials that incorporate covalently bonded $(XO_4)^{n-}$ tetrahedra (where X = P, S, B, C, Si, etc.) with a subunit of M–O polyhedra (where M = Fe, Ni Co, etc.) [13]. Polyanion framework-type materials are structurally more stable than oxides, as the oxygen atom is tightly bound to the central ion X in the tetrahedral coordination sphere. In addition to that, the presence of the inductive effect of the central metal ion in the polyanionic subunit increases the ionic character of the M–O bond, resulting in an increase in the redox potential by compelling co-active participation of the $M^{n/n+1}$ redox couple [14–16]. Transition metals such as nickel and cobalt are frequently utilized due to their electrochemically active nature in alkaline solutions. Cobalt-based phosphates exhibit pseudocapacitive behavior with high-rate performance but a reasonable amount of specific capacitance [11, 17, 19]. On the contrary, nickel-based phosphates show battery-type characteristics with higher specific capacitance/capacity compared to cobalt but are limited in rate performance [15, 20, 22]. As a result, the substitution of nickel into cobalt-based compounds can improve their overall electrochemical performance. The incorporation of Ni atoms will be a suitable way to increase active sites in the electrode material, leading to higher electrochemical performance [23, 24].

The present study reports the synthesis, characterization, and electrochemical charge storage performance of nickel-substituted potassium cobalt phosphate $KCo_{1-x}Ni_xPO_4$ $(0 \leq x \leq 0.5)$ and a detailed investigation of $KCo_{0.5}Ni_{0.5}PO_4$ as a potential robust positive electrode in a full cell in asymmetric supercapacitance (ASC) mode. The $KCo_{0.5}Ni_{0.5}PO_4$ electrode demonstrated notably enhanced electrochemical performance attributed to the synergistic effect of cobalt and nickel. The $KCo_{0.5}Ni_{0.5}PO_4$ delivers 173 mAh/g (capacitance: 1038 F/g) at a current density of 0.5 A/g in an aqueous 2 M KOH electrolyte, accompanied by cyclic stability up to 5000 cycles. The HSC mode consists of activated carbon as the negative electrode coupled with $KNi_{0.5}Co_{0.5}PO_4$ as the positive electrode, displaying high energy density and power density of 183.7 Wh/kg and 7952 W/kg, respectively, in 2 M aqueous KOH electrolyte. The superior full performance in HSC mode makes $KCo_{0.5}Ni_{0.5}PO_4$ a potential positive electrode for the development of high-performing HSCs.

2 | Experimental Procedures

2.1 | Synthesis of $KCo_{0.5}Ni_{0.5}PO_4$

The synthesis of $KCo_{0.5}Ni_{0.5}PO_4$ was done by the sol–gel autocombustion process followed by calcination of the precipitate at elevated temperatures to obtain the crystalline material shown in the Figure 1 schematics. Precursors of analytical grade were used for synthesis without any further purification. Nickel nitrate hexahydrate (Merck 99.0%), 0.5 cobalt nitrate hexahydrate (Merck 99.0%), 1 mM potassium carbonate (Merck 99.9%), ammonium phosphate (Merck 99.0%), and citric acid (Merck 99.9%) were taken in the respective molar ratios for the synthesis of $KCo_{1-x}Ni_xPO_4$. Citric acid was taken twice the total moles of Co, Ni, and K precursors in the synthesis. For the preparation of $KC_{0.5}Ni_{0.5}PO_4$, first, 0.5 mM nickel nitrate hexahydrate (Merck 99.0%), 0.5 mM cobalt nitrate hexahydrate, and 1 mM potassium carbonate (Merck 99.0%) were dissolved in 100 mL of DI water to prepare cation solution A. Then, solution B was prepared with 1 mM ammonium phosphate (Merck 99.0%). Solution B was slowly added to solution A. After that, 4 mM citric acid was added drop by drop to the cation solution to form a homogeneous metal citrate complex at 100°C. The solutions were mixed with continuous stirring for 4 h at 80°C, creating a light pinkish gel. Eventually, the reaction temperature was raised to 200°C for the combustion process. The combustion process took ~3–5 min, yielding voluminous fluffy brown material. The material was ground and kept in a muffle furnace at 400°C for 6 h. The resulting powder was transferred to a furnace and calcined at 600°C for 8 h to get crystalline $KCo_{0.5}Ni_{0.5}PO_4$. The indigo blue-colored powder was collected from the crucible, ground adequately, and utilized for further characterization and electrochemical performance studies.

2.2 | Materials Characterization

Powder XRD of all $KCo_{1-x}Ni_xPO_4$ samples was performed to examine the crystallinity and phase purity with monochromatized Cu Kα radiation (λ = 1.54056 Å) as the x-ray source in a benchtop x-ray diffractometer (Rigaku Miniflex 600) with a 10–60° 2θ range with a step size equal to 0.02°. The structure was matched using X'Pert High Score Plus (PANalytical), and the crystal structure of the materials was further refined by the Rietveld refinement method using FullProf Suite software. The morphology of the as-prepared sample $KCo_{0.5}Ni_{0.5}PO_4$ was characterized using an EVO—Scanning Electron Microscope (MA15/18 CARL ZEISS). FT-IR spectra were recorded in the wavenumber range of 400–4000 cm^{-1} to understand the presence of functional groups in the prepared sample using an FT-IR spectrometer (Nicolet 6700, Thermo Scientific). The elemental composition and their electronic states present in the sample were examined by x-ray photoelectron spectroscopy (XPS), measured using a Thermo Scientific instrument with a monochromatic Al Kα x-ray source. A Brunauer–Emmett–Teller (BET) analyzer was used to determine the specific surface area of the $KCo_{0.5}Ni_{0.5}PO_4$ sample using a BELSORP-II (Microtrac BEL Japan) with the help of N_2 adsorption/desorption isotherms at 77 K.

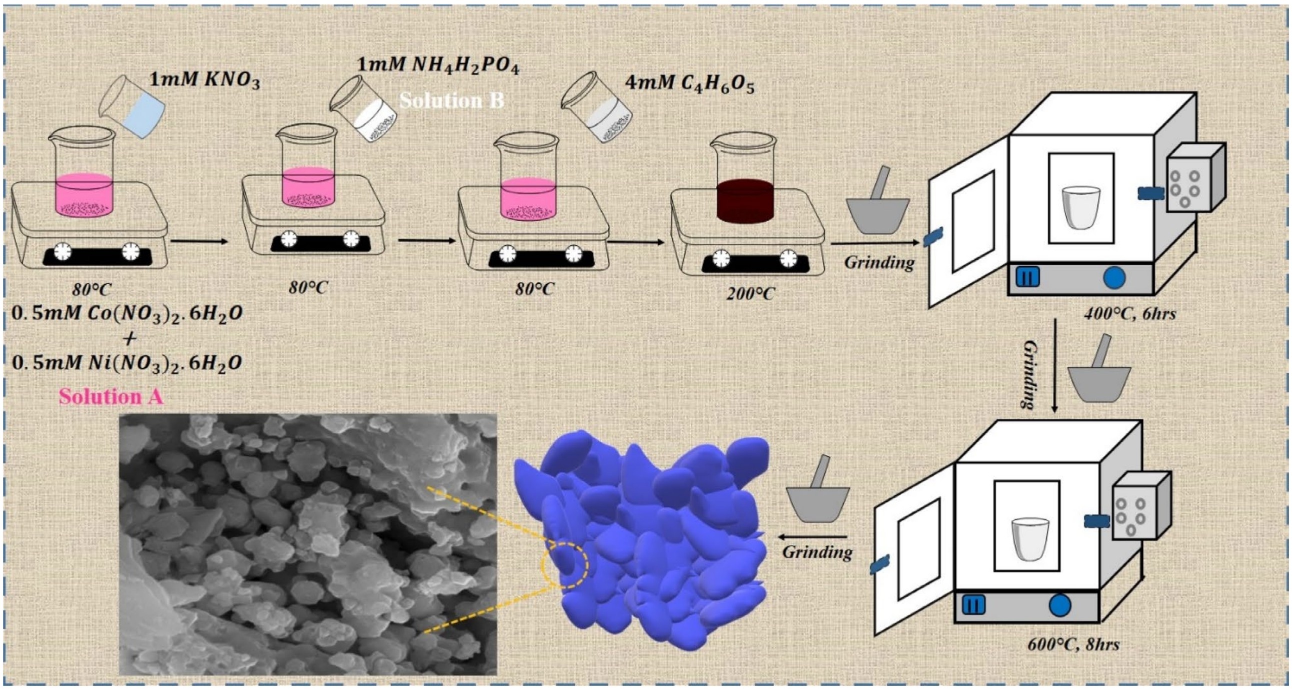

FIGURE 1 | Schematic of synthesis of the $KCo_{0.5}Ni_{0.5}PO_4$ sample.

To investigate the electrochemical properties of the synthesized $KCo_{0.5}Ni_{0.5}PO_4$ sample, cyclic voltammetry (CV), galvanostatic charge–discharge (GCD), and electrochemical impedance spectroscopy (EIS) were performed using a conventional three-electrode system and measured with a Metrohm Autolab (PGSTAT204) coupled with an FRA32M module for impedance analysis. NOVA1.1 software was used to analyze the electrochemical measurements.

2.3 | Electrode Preparation

Electrochemical measurements were performed in a three-electrode electrochemical cell, which involved $KCo_{1-x}Ni_xPO_4$ ($x = 0$, 0.1, 0.3, and 0.5) as the working electrode, a saturated calomel electrode (SCE) as the reference electrode, and a platinum plate as the counter electrode. The working electrode was prepared in 70:20:10 wt% for the active material ($KCo_{1-x}Ni_xPO_4$), conducting carbon (acetylene black, Alfa Aesar), and binder (PVDF, Merck), respectively, in NMP (N-methyl-2-pyrrolidone) solvent. The homogeneous slurry was made in an agate mortar pestle. This slurry mixture, containing ~1 mg of active material, was coated onto a 1 cm^2 area of Toray carbon paper (Alfa Aesar). It was followed by drying at 80°C for 12 h to obtain the working electrode. After that, the weight of the loaded electrode material was calculated by taking the difference between the weight of the material-loaded electrode and the weight of the blank electrode (Shimadzu electronic weighing balance machine, error limit: 0.01 mg). As-prepared, dried electrodes were used for further study of electrochemical measurements. In the full cell (HSC mode), electrochemical studies were performed using activated carbon as the counter/reference electrode in 2 M KOH electrolyte.

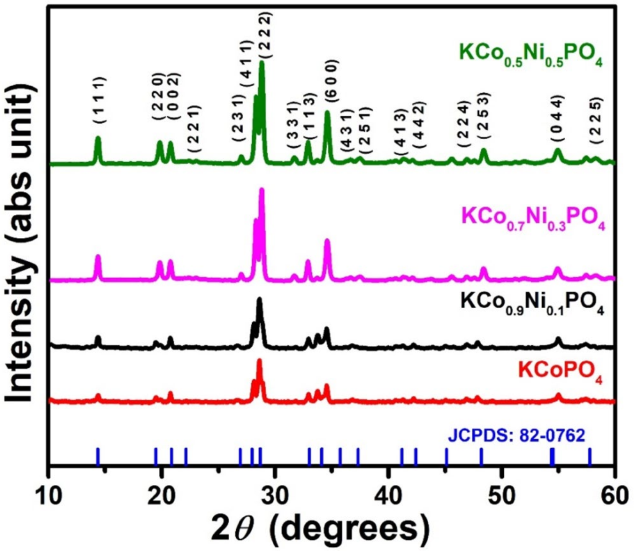

FIGURE 2 | Powder XRD pattern of $KCo_{1-x}Ni_xPO_4$ ($x = 0$, 0.1, 02, 0.3, 0.4, and 0.5).

2.4 | Results and Discussion

The powder XRD pattern of $KCo_{1-x}Ni_xPO_4$ ($x = 0$, 0.1, 0.3, and 0.5) samples calcined at 600°C is presented in Figure 2. XRD peaks of all the samples match well with JCPDS no.: 82-0762 of hexagonal $KCoPO_4$. Rietveld refined powder XRD profile of calcined $KCo_{0.5}Ni_{0.5}PO_4$ is shown in Figure 3a, which matches the reference structure (JCPDS No.: 82-0762 of $KCoPO_4$) without observing any impurity peaks. Refined cell parameters ($a = 18.021660$, $b = 18.021660$, and $c = 8.604042$) and $R_p = 17.5$, $R_{wp} = 11.4$, $R_{exp} = 8.78$, and $\chi^2 = 1.67$ represent the hexagonal crystal structure

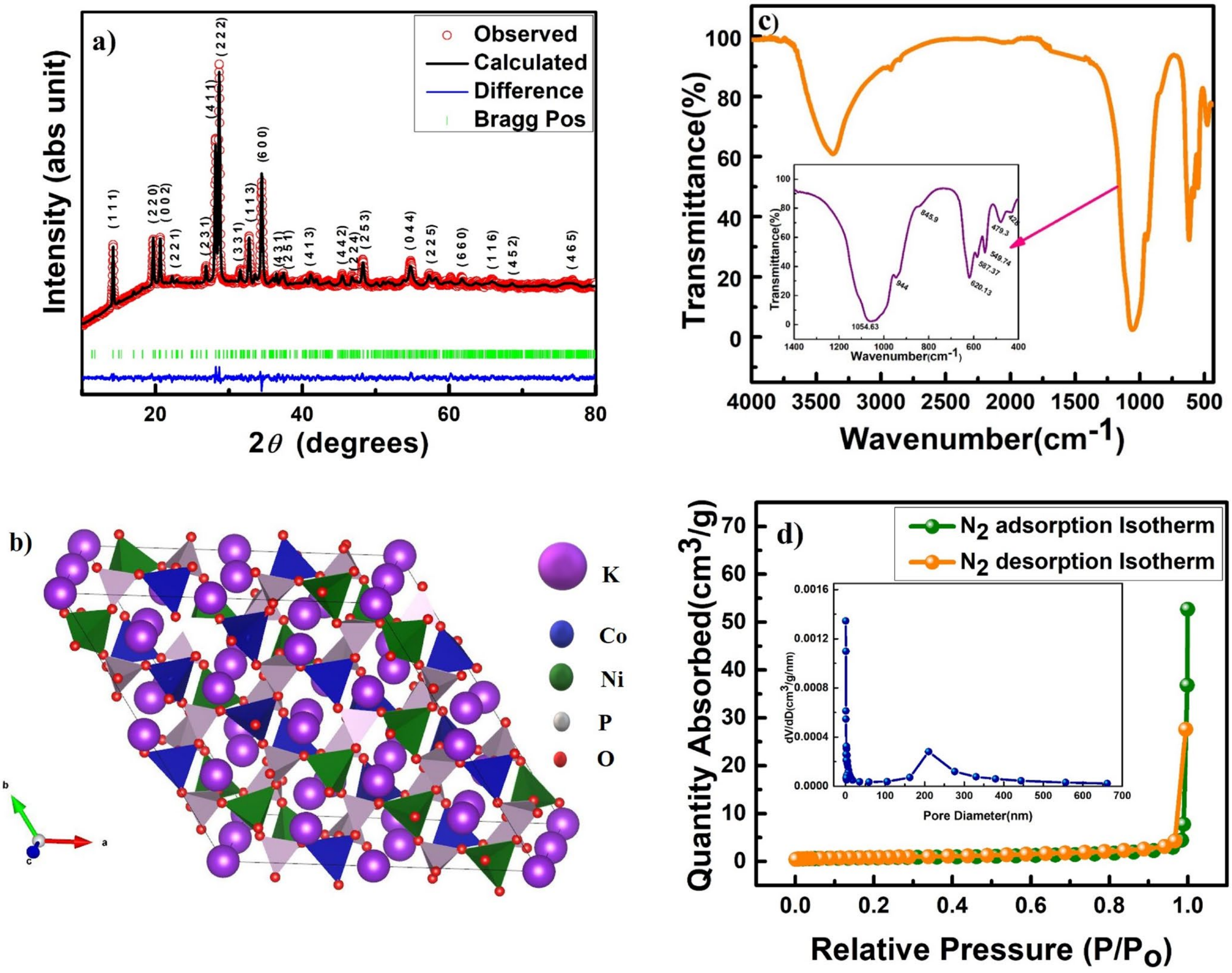

FIGURE 3 | (a) XRD Rietveld refinement pattern of the $KCo_{0.5}Ni_{0.5}PO_4$ powder sample, (b) VESTA image of $KCo_{0.5}Ni_{0.5}PO_4$ (blue, green, and gray are tetrahedra of Co–O, Ni–O, and P–O, respectively), (c) FTIR spectrum of $KCo_{0.5}Ni_{0.5}PO_4$, and (d) N_2 adsorption/desorption isotherm of the $KCo_{0.5}Ni_{0.5}PO_4$ sample.

formation with space group P63. Similarly, the refinement of another prepared sample of $KCo_{1-x}Ni_xPO_4$ ($x = 0$, 0.1, 0.3, and 0.5) is shown in Figure S1. The presence of Co–O and Ni–O polyhedra, shared and connected by corner sharing oxygen of phosphate, is confirmed by the VESTA image displayed in Figure 3b. The ionic radius of Ni^{2+} is smaller than that of Co^{2+} in tetrahedra. The substitution of Ni^{2+} ions at the Co^{2+} site enhances the entropy of the system, which reduces the growth of large crystallites. That is why, when substitution increases up to 50%, the grown crystallites are in the range of nanometer sizes, as confirmed by SEM, TEM study, and crystallite sizes calculated using Debye–Scherrer's equation from XRD peak broadening [25].

The FTIR spectra of $KCo_{0.5}Ni_{0.5}PO_4$ powder samples, recorded between the wavenumber ranges of 400-4000 cm^{-1}, are shown in Figure 3c. The broad peak at 3400 cm^{-1} in the $KCo_{0.5}Ni_{0.5}PO_4$ spectra implies the stretching vibration of a hydroxyl group (ν (–OH)), signifying the presence of water in the compound. In the FTIR spectra, a strong band appeared at 1054.83 cm^{-1} due to the asymmetric stretching (ν_{as}) of the P–O bond vibration (990-1200 cm^{-1}), and symmetric stretching (ν_{ss}) vibration of P–O resulted in a strong transmittance peak at 944 and 845.9 cm^{-1} for the $-PO_4$ group [26]. Peaks at 620 cm^{-1} correspond to O–P–O out-of-plane bending, and those at 428 cm^{-1} correspond to the $-\delta PO_4$ group. Thus, the major vibrational spectra validate the presence of the $-PO_4$ group in $KCo_{0.5}Ni_{0.5}PO_4$. The asymmetric stretching modes of CoO_6 octahedra have been observed at 587 cm^{-1} [27]. The peak around 549 cm^{-1} may be ascribed to the asymmetric stretching of Ni–O bonds in NiO_6 octahedra [28]. The absorption peak at 479 cm^{-1} is also attributed to both Ni–O and Co–O bonding present in the prepared sample $KCo_{0.5}Ni_{0.5}PO_4$ [29].

Indeed, to analyze the surface area and pore volume of the sample, the N_2 adsorption–desorption isotherm carried out at 77 k is shown in Figure 3d. It represents a type III isotherm with a hysteresis loop of H3 type, implying the presence of mesoporous structures connected via macropores [30, 31]. The small hysteresis in the high relative pressure range in the N_2 adsorption–desorption isotherm indicates the capillary condensation phenomenon, indicating the mesoporous nature [32]. Moreover, the specific surface area of the prepared sample is equivalent to 25.875 m^2/g, with the major pore size distribution in the range of 3 to 10 nm and some macropores (~220 nm), obtained by BJH (Brunauer, Joyner, and Halenda) plot (inset of Figure 3d).

Mesopores are attributed to the good electrochemical performance of the materials because of their high porosity. The calculated average pore diameter of the $KCo_{0.5}Ni_{0.5}PO_4$ sample was found to be ~20.79 nm.

The chemical composition and valence state of constituent elements of the $KCo_{0.5}Ni_{0.5}PO_4$ sample were examined by the XPS. The wide-range survey spectrum shown in Figure 4a confirms the presence of K Co, Ni, P, and O in the sample. Moreover, Figure 4b shows the binding energies of K $2p_{3/2}$ and K $2p_{1/2}$ states at 292.2 and 295.1 eV, respectively, confirming the presence of K^+ ions in the sample. The Co(2p) spectrum shown in Figure 4c splits into different peaks, corresponding to $2p_{3/2}$ of Co^{2+} at 780.63 eV and $2p_{1/2}$ of Co^{2+} at 796.41 eV, as well as satellite peaks at 784.17 and 801.96 eV that arise from Co^{2+} ions. The core-level spectrum of Ni(2p) is shown in Figure 4d and is deconvoluted into Ni $2p_{3/2}$ and Ni $2p_{1/2}$ states at the binding energies of 855.6 and 873.4 eV, respectively, with corresponding satellite peaks at 860.9 and 879 eV. These binding energies confirm Ni as Ni^{2+} in the sample. O(1 s) state of the $KCo_{0.5}Ni_{0.5}PO_4$ sample has two prominent peaks shown in Figure 4e at 530.8 eV for the metal-oxygen bond of (Ni–O, Co–O) and 532.2 for P–O bonding, respectively [33]. The P(2p) peak, de-convoluted into $2p_{3/2}$ and P $2p_{1/2}$ in Figure 4f, is observed at binding energies at 132.41 and 133.47 eV, respectively, confirming P^{5+} ions in the -PO_4 unit.

The morphological characterization of the prepared $KCo_{1-x}Ni_xPO_4$ ($x = 0$, 0.1, 0.3, and 0.5) sample was observed by electron microscopy techniques. Figure 5a represents the FE-SEM image of the sample, displaying the particle morphology and surface structure of the $KCo_{0.5}Ni_{0.5}PO_4$ powder sample, suggesting an average particle size of 437 nm with flake-like arrangements. Elemental analysis of the $KCo_{0.5}Ni_{0.5}PO_4$ sample is shown in Figure 5b in the form of an energy dispersive x-ray analysis (EDX) image, which shows the peaks of all elements such as K Co, Ni, P, and O present in $KCo_{0.5}Ni_{0.5}PO_4$. Further, FESEM mapping of the prepared sample is shown in Figure 5c–g and confirms that K, Co, Ni, P, and O are distributed throughout the electrode material present in their purest form on the synthesized product. Similarly, Figures S2–S4 represent the FE-SEM image of $KCo_{1-x}Ni_xPO_4$ for $x = 0$, 0.1, and 0.3, with particle size distribution. Subsequently, the introduction of Ni in $KCo_{1-x}Ni_xPO_4$ has a significant effect on the morphology of the sample, as the average particle size reduces in order of Ni doping in $KCo_{1-x}Ni_xPO_4$ ($x = 0 > 0.1 > 0.3 > 0.5$) [25]. Additionally, EDX along with elemental mapping of $KCo_{1-x}Ni_xPO_4$ for $x = 0$, 0.1, and 0.3 was performed to understand the composition of doping in a prepared sample.

High-resolution transmission electron microscopy (HRTEM) images of the $KCo_{0.5}Ni_{0.5}PO_4$ sample are shown in Figure 6a, which represents the lattice fringes of the sample. Figure 6a(i–ii) shows the FFT (fast Fourier transformation) and inverse FFT images. Figure 6b shows the thickness of the lattice fringes, with the calculated d spacing of 0.252 nm matching very well with the (600) plane of the prepared sample $KCo_{0.5}Ni_{0.5}PO_4$.

2.5 | Electrochemical Studies

Cyclic voltammogram (CV plots) of all the $KCo_{1-x}Ni_xPO_4$ ($x = 0$, 0.1, 0.3, and 0.5) samples in 2 M KOH electrolyte is shown in Figure 7 for comparison at a scan rate of 5 mV/s in the voltage range of 0–0.6 V. The CV plot of $KCoPO_4$ shows capacitive charge storage with a near-rectangular-type CV

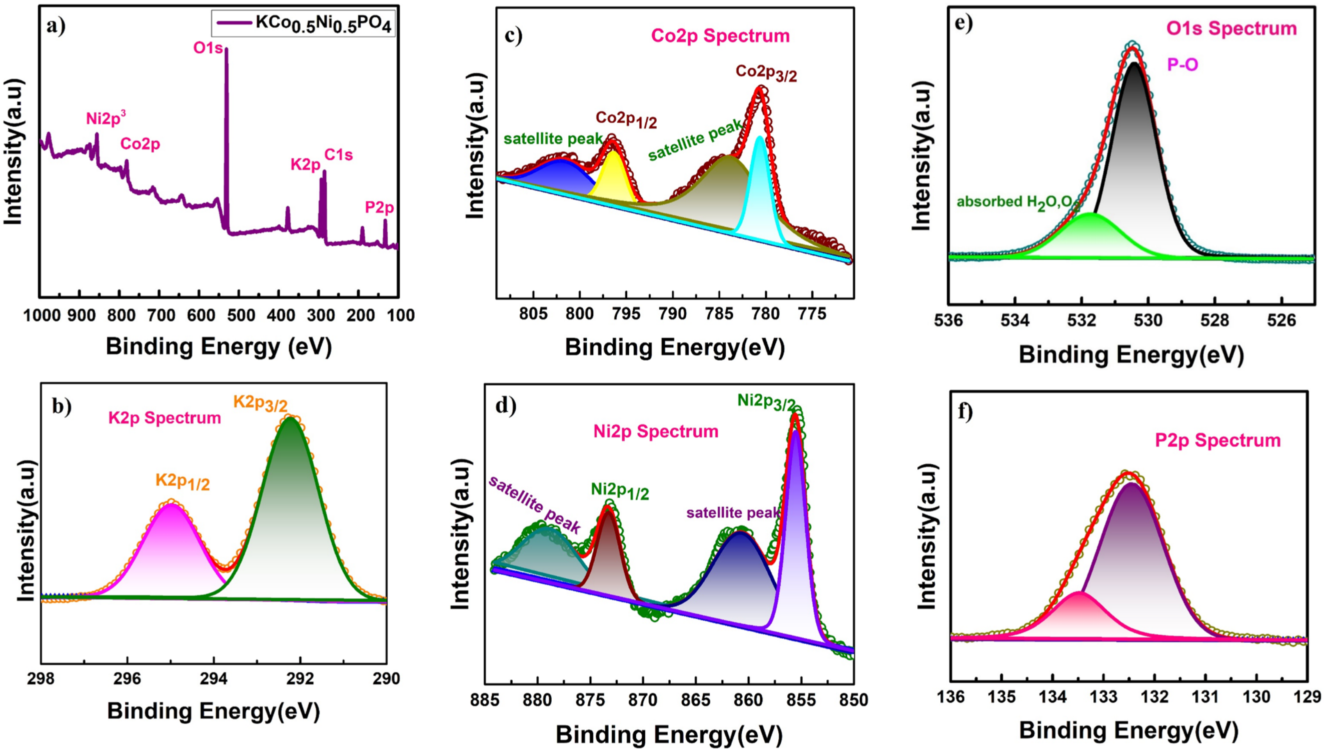

FIGURE 4 | XPS of the $KCo_{0.5}Ni_{0.5}PO_4$ powder sample: (a) full survey, (b) K (1 s), (c) Co(2p), (d) Ni(2p), (e) O (1 s), and (f) P (2p).

curve. Redox peaks start appearing in the CV plot after Ni doping in the samples. As Ni content increased in the sample, the redox peak intensity increased, along with the increased area under the CV curve, representing an increase in the charge storage capacity of Ni-doped $KCoPO_4$ samples. The charge storage capacity of the electrode materials was calculated using Equation (1) to examine the electrochemical characteristics of the prepared sample.

$$C_{sp} = \frac{\int i(V)dV}{2mV\vartheta} \tag{1}$$

The specific charge storage capacity in mAh/g can be calculated using Equation (2).

$$C\left(\frac{\text{mAh}}{\text{g}}\right) = C_{sp} \times \Delta V = \frac{\int i(V)dV}{2m\vartheta \times 3.6} \tag{2}$$

where 'm' is the active mass of the electrode (g), 'V' is the operating voltage window (V), and 'ϑ' is the scan rate (mV/s). The charge storage capacity of $KCo_{1-x}Ni_xPO_4$ ($x=0$, 0.1, 0.3, and 0.5) samples was found to be 575, 623, 735, and

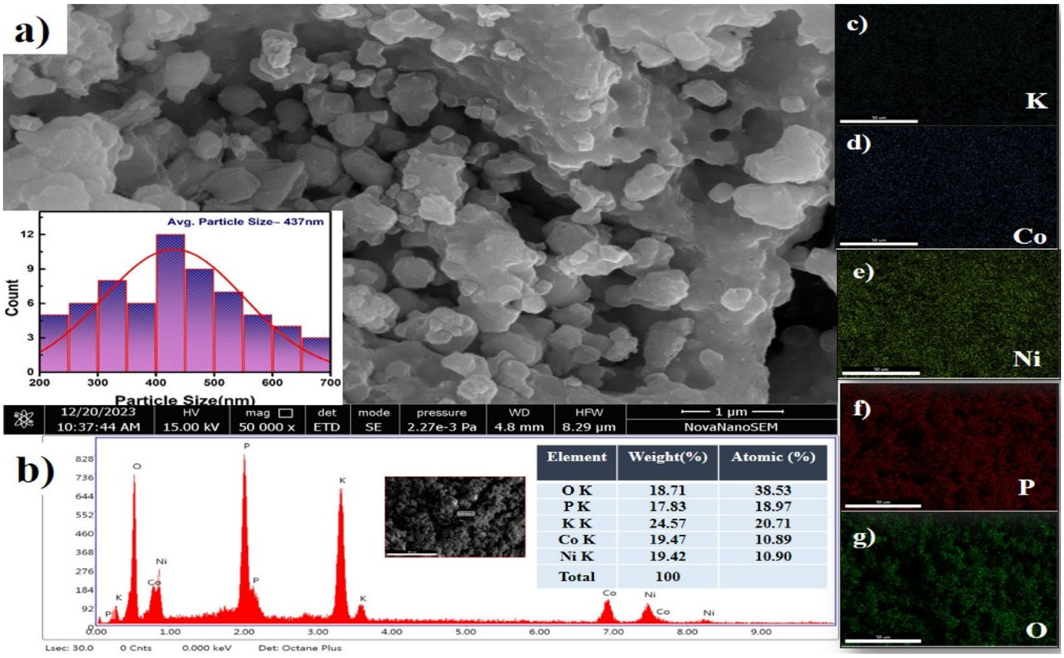

Element	Weight(%)	Atomic (%)
O K	18.71	38.53
P K	17.83	18.97
K K	24.57	20.71
Co K	19.47	10.89
Ni K	19.42	10.90
Total	100	

FIGURE 5 | (a) Particle distribution of $KCo_{0.5}Ni_{0.5}PO_4$ in SEM image, (b) elemental analysis of $KCo_{0.5}Ni_{0.5}PO_4$ by EDX, and (c)–(g) color mapping of the elements present in $KCo_{0.5}Ni_{0.5}PO_4$.

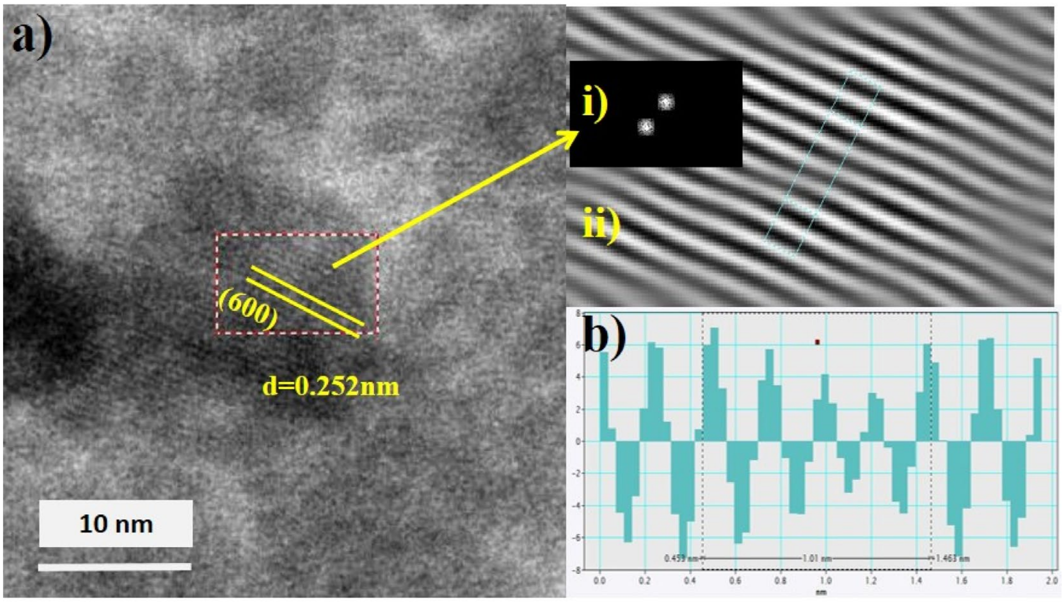

FIGURE 6 | (a) Visible lattice fringes containing 600 planes in the HRTEM image, (i–ii): FFT and inverse FFT images of the selected region of the (600) plane. (b) d spacing of fringes that matches with the (600) plane of the $KCo_{0.5}Ni_{0.5}PO_4$ lattice.

845 F/g, respectively, at the scan rate of 5 mV/s in 2 M KOH electrolyte. The highest charge storage performance along with a distinctive redox peak was observed for the $KCo_{0.5}Ni_{0.5}PO_4$ sample. That is why, the investigation of the electrochemical performance of $KCo_{0.5}Ni_{0.5}PO_4$ as the working electrode was carried out by CV, GCD study, and impedance spectroscopy (EIS) in a three-electrode arrangement in 2 M KOH as the electrolyte. In Figure 8a, the CV curves at various scan rates exhibit redox peaks between the potential range of 0–0.6 V. Figure 8a shows the CV curve of $KCo_{0.5}Ni_{0.5}PO_4$; the nature of the curve presents the redox-mediated intercalating storage coupled with surface redox (electrosorption) behavior. The nature of the CV curve nature confirms the intercalative type of redox-mediated storage. The redox peaks result from the reversible interconversion of both $Co^{2+/3+}$ and $Ni^{2+/3+}$ through electrosorption of OH^- ions, as represented by Equation (1).

$$\begin{gathered}KCo_{0.5}((II))Ni((II))_{0.5}PO_4 + OH^-{}_{sol} \leftrightarrow KCo((III))_{0.5}Ni_{0.5}((III))\ (OH^-)PO_4 \\ (\text{redox} - \text{mediated diffusion controlled intercalation})\end{gathered} \tag{3}$$

EDLC-type surface capacitance:

$$KCo_{0.5}((II))Ni((II))_{0.5}PO_4 + xKOH \leftrightarrow K^+{}_x|KCo_{0.5}((II))Ni((II))_{0.5}PO_4|xOH^- \tag{4}$$

Total charge storage capacity:

$$\begin{gathered}KCo_{0.5}((II))Ni((II))_{0.5}PO_4 + KOH + OH^-{}_{sol} \leftrightarrow K^+{}_x|KCo_{0.5}((II)) \\ Ni((II))_{0.5}PO_4|OH^-{}_{(1+x)}\end{gathered} \tag{5}$$

The charge storage capacity of $KCo_{0.5}Ni_{0.5}PO_4$ was calculated using Equations (1) and (2), and the charge storage capacity was found to be close to 142.3 mAh/g (capacitance: 854 F/g) at 0.5 mV/s scan rate. The shifting of the anodic and cathodic peaks was observed linearly with increasing scan rate, confirming the dominance of diffusion-controlled intercalative type of redox-mediated charge storage in the materials. Figure 8b shows the relation of anodic and cathodic peak currents linearly with the square root of the scan rate, confirming that the $KCo_{0.5}Ni_{0.5}PO_4$ electrode exhibits a semi-infinite diffusion-controlled redox reaction. The kinetics of the electrodes can be examined by determining the ion diffusion coefficient. The ion diffusion coefficient of the electrode was calculated using the Randles–Sevick equation presented below [34, 35].

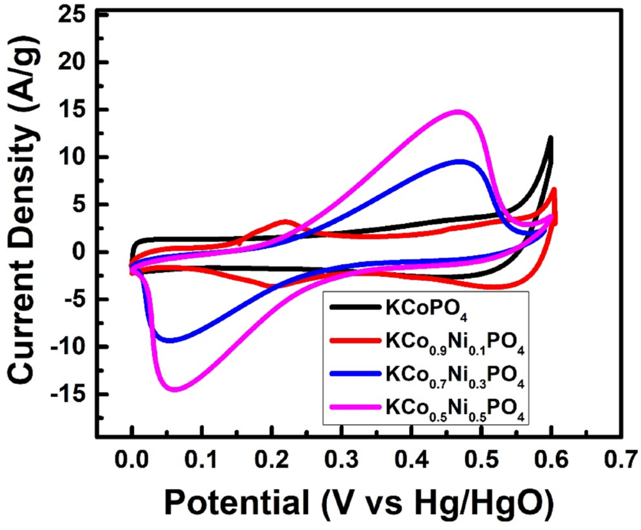

FIGURE 7 | Comparative CV of $KCo_{1-x}Ni_xPO_4$ (x = 0, 0.1, 0.3, and 0.5) in 2 M KOH electrolyte solution and 5 mV/s scan rate.

$$i_p = 2.686 \times 10^5 \times n^{3/2} AD^{1/2} C_o v^{1/2} \tag{6}$$

where i_p is peak current density (A), n is the number of electrons that participated in the redox reaction (usually 1), A is the area of the electrode in cm^2, D is the diffusion coefficient in cm^2/s, C_o is the OH^- ion concentration in mol/cm^3, and ν is the scan rate in V/s. Using Equation (6), the diffusion coefficient of OH^- in the $KCo_{0.5}Ni_{0.5}PO_4$ electrode was found to be $1.47 \times 10^{-8}\,cm^2/s$ for the oxidation reaction and $1.38 \times 10^{-8}\,cm^2/s$ for the reduction reaction.

To qualitatively understand the electrochemical kinetics, a power-law equation was used, given below in Equation (7) [34].

$$i = av^b \tag{7}$$

a and b are adjustable parameters, i is the current (A), and ν is the scan rate (V/s). The b values lie between 0.5 to 1, b equal to 0.5 for the intercalative semi-infinite diffusion-controlled redox process or battery-type charge storage behavior, while b equal to 1 represents the surface-controlled charge storage. Figure 8c shows the log[peak current (i_p) vs. log (ν) plots], and from the slope of the plot, b values are extracted. The b-values of current observed for oxidation and reduction were close to 0.623 and 0.651, respectively, suggesting that the charge storage mechanism in $KCo_{0.5}Ni_{0.5}PO_4$ is a semi-infinite diffusion-controlled intercalating process rather than capacitive.

The scan rate dependence on the current density plot, which can quantitatively determine the contribution of the capacitive and intercalation of ions at low scan rates, is shown in Figure 8d. Dunn's method quantitatively separates the capacitive and diffusion-controlled charge storage in the electrodes into two components using Equation (8) [15, 29, 36].

$$i(\upsilon) = k_1 \nu + k_2 \nu^{\frac{1}{2}} \tag{8}$$

Equation (8) was simplified into Equation (9) to separate the total charge stored into the respective contributions.

$$i(\upsilon) / \nu^{(1/2)} = k_1 / \nu^{(1/2)} + k_2 \tag{9}$$

From Equation (9), k_1 and k_2 explain the contribution of current from the surface capacitance and diffusion-controlled intercalation charge storage, respectively. Consequently, the current response $i(V)$ is from CVs for a range of scan rates, and the slope of a linear fit offers a constant k_1 and y-axis intercept for the constant k_2, when plotted $i(V)/\nu^{1/2}$ versus $\nu^{1/2}$, as displayed in Figure 9d. As shown in Figure 8e, after the calculation of k_1 and

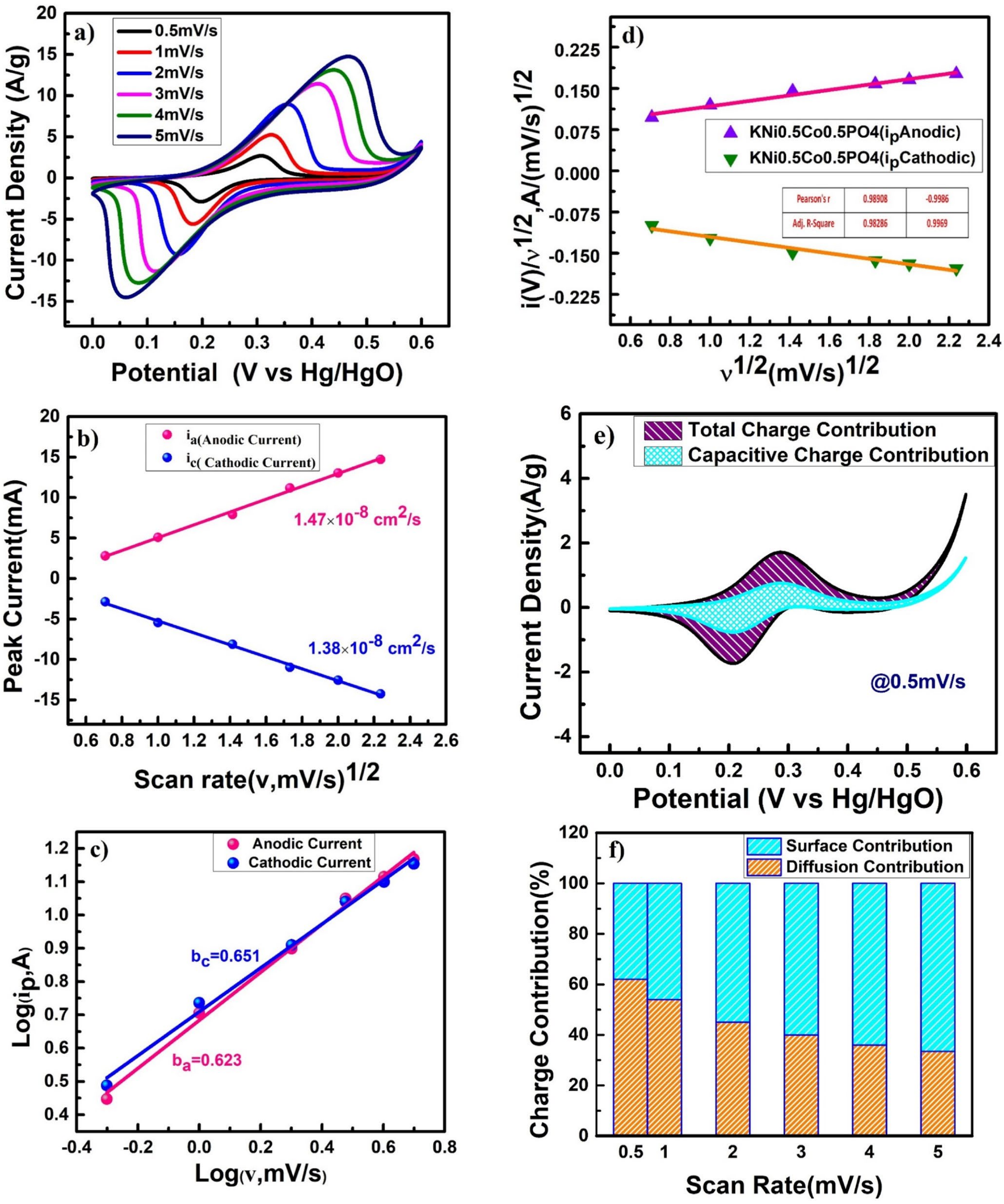

FIGURE 8 | (a) Cyclic voltammetry of $KCo_{0.5}Ni_{0.5}PO_4$ electrode in 2 M KOH electrolyte, (b) peak current density vs. square root of the scan rates plot, (c) plot of log (peak current) vs. log (scan rate) presenting *b* values, (d) capacitive and diffusion control process contribution in the current density at the scan rate of 0.5 mV/s, (e) surface capacitance and diffusion-controlled interaction process contribution at a scan rate of 0.5 mV/s on the charging peak potential equal to 0.31 V, and (f) capacitive and diffusion control process contribution at different scan rates.

k_2 values, the contribution of surface-controlled charge storage was close to 37.7%, and the contribution from the diffusion-controlled interaction process was close to 62.3% at 0.31 V peak potential with a 0.5 mV/s scan rate. The contribution of diffusion-controlled intercalative and surface-controlled charge storage at various scan rates is shown in Figure 8f.

According to Trassati, the sum of the contributions from the electrode's inner and outer surfaces determines a material's overall charge storage capacitance and is represented by Equation (10) [11, 15, 34].

$$C_{\text{total}} = C_{\text{in}} + C_{\text{out}}\ (\text{F}/\text{g}) \tag{10}$$

The total charge storage capacitance contribution from the inner and outer surface of the electrode is dependent on the square root of the scan rate. The total charge stored at the electrode or the total capacitance of the electrode is measured by the y-intercept of the linear fit of C^{-1} vs. $\nu^{1/2}$ at different scan rates, as shown in Figure 9a. Further, the y-intercept of the linear C vs. $\nu^{1/2}$ curve determines the outer surface contribution to charge storage or outer capacitance (C_{out}) of the electrode, as displayed in Figure 9b. Using the Trasatti plot, the total amount of charge stored in the electrode was found to be close to 142.3 mAh/g (capacitance: 854 F/g) at 0.5 mV/s, in which the inner surface contribution and outer surface contribution in total capacitance, C_{in} was found to be 91 mAh/g or 546 F/g (64% of total capacity) and C_{out} was found to be 51.3 mAh/g (capacitance: 308 F/g [36% of total capacity]), respectively. Overall, it can be concluded that the electrode stores charge primarily by the semi-infinite diffusion-controlled mechanism [37].

GCD analysis was performed within the potential window 0–0.6 V at constant and different current density values to further analyze the charge storage performance. From the GCD curves at numerous discharge currents, the electrode's charge storage capacity (total capacitance) can be calculated using Equation (11) [38, 39].

$$C_{\text{sp}} = \frac{I\Delta t}{m\Delta V} \tag{11}$$

The specific capacity of the electrode in mAh/g is calculated by modifying Equation (11) as represented below.

$$C\left(\frac{\text{mAh}}{\text{g}}\right) = C_{\text{sp}} \times \Delta V = \frac{i\Delta t}{m \times 3.6} \tag{12}$$

where I is the discharge current density (A), Δt is the discharge time (s), m is the active mass of the electrode (g), and ΔV is the potential window of the discharge (V).

Figure 10a depicts the Galvanostatic capacity/capacitances of $KCo_{0.5}Ni_{0.5}PO_4$, and the values are found close to 173 mAh/g (capacitance: 1038 F/g), 144.3 mAh/g (capacitance: 865.8 F/g), 115.5 mAh/g (capacitance: 693 F/g), 85.8 mAh/g (capacitance: 515 F/g), 61.2 mAh/g (capacitance: 367.6 F/g), and 37.4 mAh/g (capacitance: 224.4 F/g) at current rates of 0.5, 1, 2, 3, 4, and 5 A/g. The GCD curves of $KCo_{0.5}Ni_{0.5}PO_4$ electrodes exhibit a stable and symmetric charging and discharging nature, which indicates that the electrode shows a pseudocapacitive nature, which originates from redox-mediated intercalating storage. Higher capacity was observed in GCD experiments compared to CV, suggesting more diffusion-controlled bulk charge storage of the material, confirming the redox-mediated battery-type intercalating charge storage in the material. The specific capacity of $KCo_{0.5}Ni_{0.5}PO_4$ is measured at different current densities from 0.5 to 5 A/g with cycle number, as presented in Figure 10b. With the increase in current rates, the charge storage capacity of the material decreased. It is worth noting that when the current density is reversed back to 1 A/g after testing at different rates, it clearly shows that the specific capacity of $KCo_{0.5}Ni_{0.5}PO_4$ is stable. Figure 10c presents the superior cycle stability of $KCo_{0.5}Ni_{0.5}PO_4$ electrodes at 5 A/g for 5000 cycles. It was observed that 88.93% of capacity retention after 5000 cycles. Simultaneously, Figure 10c also displays the coulombic efficiency ($\eta = {}^{t_d}/{}_{t_c}$) of the electrode, and it was found to be ~97.2% after 5000 cycles of charge/discharge, suggesting the superior reversibility and robust performance of the $KCo_{0.5}Ni_{0.5}PO_4$ electrode. Further, EIS was conducted to investigate the electrochemical performance of the $KCo_{0.5}Ni_{0.5}PO_4$ electrode during long-term application. EIS spectra are shown as Nyquist plots in Figure 10d for the $KCo_{0.5}Ni_{0.5}PO_4$ electrode before and after the cycling stability test, within the frequency range from 100 kHz to 0.1 Hz at 10 mV of the applied potential. The solution resistance (R_s) has suffered a very minute change (from 1.23 to 1.52 Ω). The charge transfer resistance (R_{ct}), which describes the accumulation of electrolyte ions across the KOH/ $KCo_{0.5}Ni_{0.5}PO_4$ interface, increased from 0.55 to 0.81 Ω. The total resistance (a summation of R_s and R_{ct}), representing the equivalent series

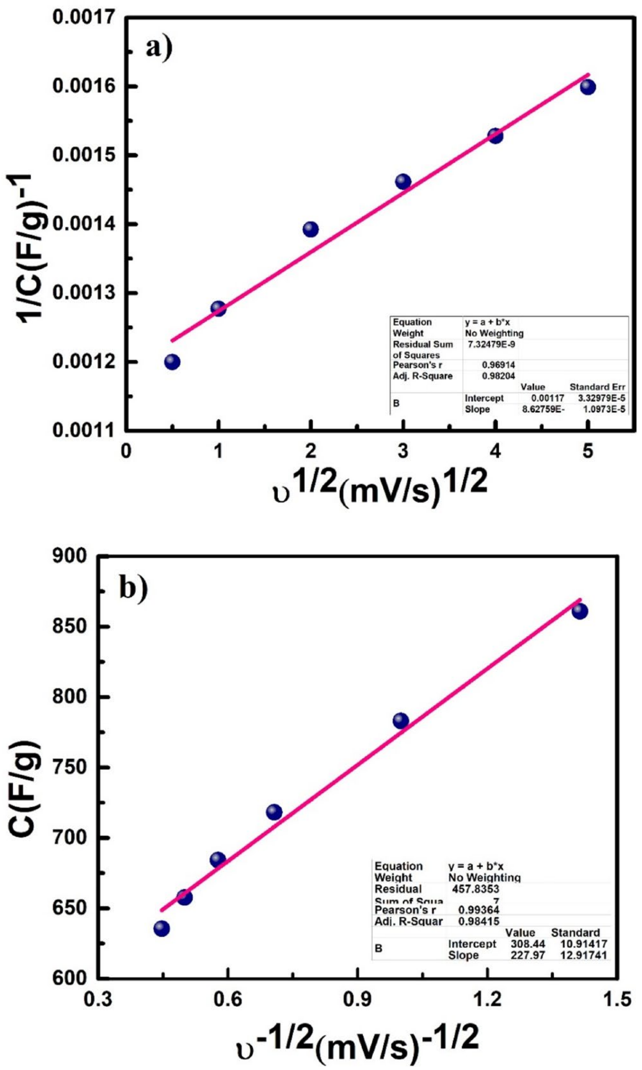

FIGURE 9 | (a) C^{-1}vs. $\nu^{1/2}$, (b) C vs. $\nu^{-1/2}$ derived from Trasatti's method.

resistance (ESR), an important parameter for generally evaluating storage materials [36]. In this particular instance, the $KCo_{0.5}Ni_{0.5}PO_4$ electrode's ESR increased little (from 1.78 to only 2.35 Ω), demonstrating the $KCo_{0.5}Ni_{0.5}PO_4$ material's superior performance.

2.6 | Full-Cell Measurements in HSC Mode

An HSC was fabricated to demonstrate the practical application, employing $KCo_{0.5}Ni_{0.5}PO_4$ as the positive electrode and activated carbon (AC) as the negative electrode in a 2 M KOH electrolyte. To obtain the highest charge storage capacity in the full-cell test, the storage capacity of both electrodes was balanced using the equation presented below:

$$\frac{1}{C_{\text{total}}} = \frac{1}{C_{\text{positive}}} + \frac{1}{C_{\text{negative}}} \tag{13}$$

In a two-electrode system, the optimal mass ratio (m^+/m^-) of the positive electrode and the negative electrode can be calculated according to the equation:

$$\frac{m^-}{m^+} = \frac{C_+ \times \Delta E_+}{C_- \times \Delta E_-} \tag{14}$$

where m^+, m^-, C_+, C_-, and ΔE_+, ΔE_- are both electrodes' active mass, specific capacitance, and potential window.

Figure 11a shows the independent CVs of AC (activated carbon) (the negative electrode) and $KCo_{0.5}Ni_{0.5}PO_4$ (the positive electrode). The active mass ratio ($\frac{m^-}{m^+}$) of electrodes was found to be 3.1: 1. Figure 11b demonstrates the CV curve of the AC// $KCo_{0.5}Ni_{0.5}PO_4$ full cell in two-electrode HSC mode in the potential window of 1.6 V with different scan rates from 1 to 100 mV/s. Subsequently, Figure 11c, shows the quantitative charge storage ability of the full cell using the GCD plot. The capacity/capacitance value was calculated using Equation (10), and the charge storage capacity of the full HSC was found to be 228.3 mAh/g (capacitance: 514 F/g), 174.8 mAh/g (capacitance: 394 F/g), 112.5 mAh/g (capacitance: 254 F/g), 77.2 mAh/g (capacitance:173.7 F/g), and 45.57 mAh/g (capacitance: 102.5 F/g) at respective current rates of 0.5, 1, 2.5, 5, and 10 A/g. Figure 11d depicts the EIS spectra (Nyquist plot) in the frequency range

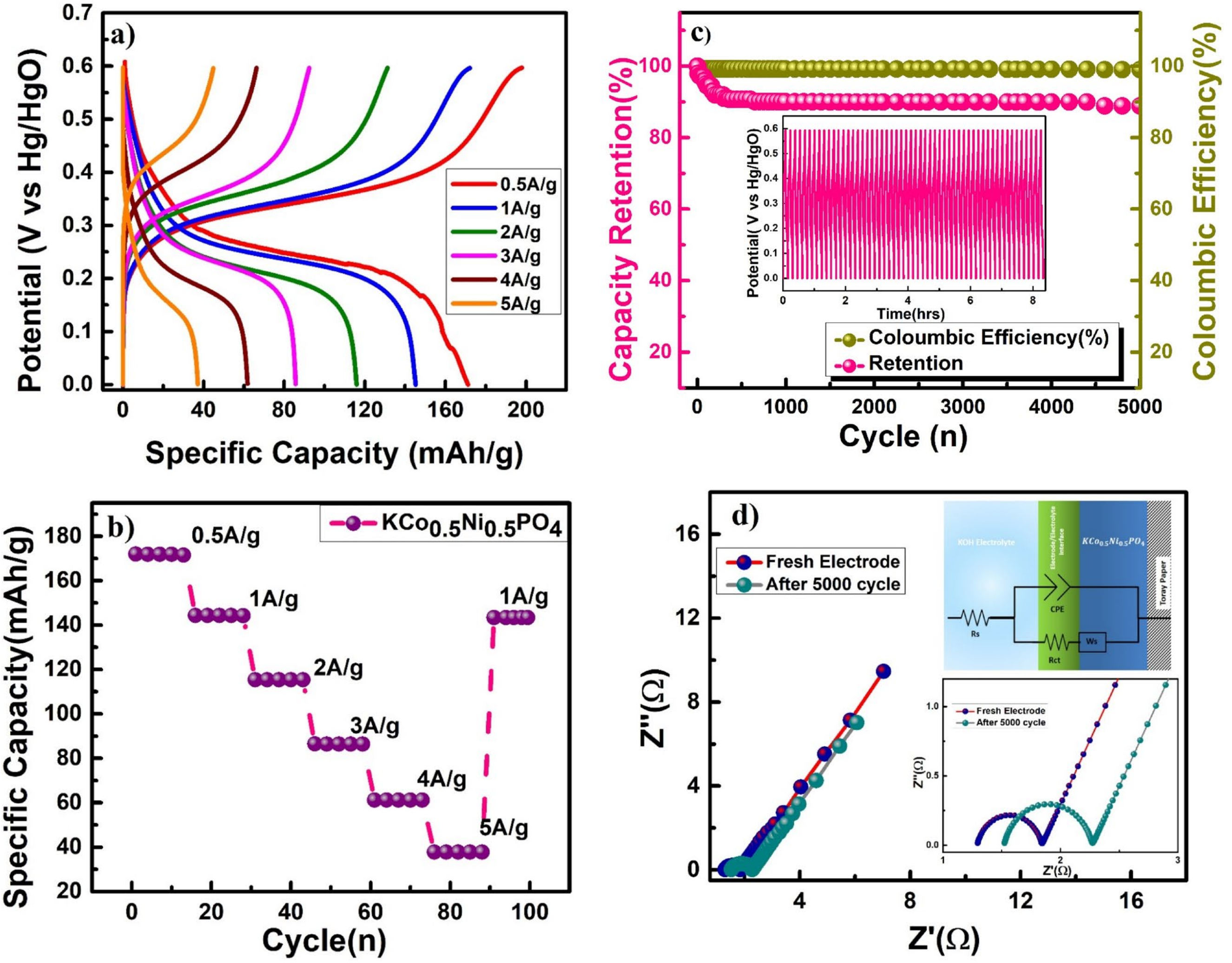

FIGURE 10 | (a) Charge/discharge plot (V vs. time) of the $KCo_{0.5}Ni_{0.5}PO_4$ electrode at various constant current rates (0.5, 1, 2, 3, 4, and 5 A/g), (b) capacity/capacitance performance of the $KCo_{0.5}Ni_{0.5}PO_4$ in 2 M KOH electrolyte at different current densities, (c) capacity retention and Coulombic efficiency plot, and (d) Nyquist plot before and after cycle at 10 mV applied voltage in the frequency range of 1 MHz to 0.1 Hz.

(1 MHz to 0.1 Hz) at 10 mV/s of applied potential before and after cyclability. According to the Nyquist plot, before and after cyclability, the value of solution resistance $R_s = 1.44$ and $2.12\,\Omega$ respectively, accompanied by the charge transfer resistances of the device being $R_{ct} = 5.03\,\Omega$ (before) and $R_{ct} = 7.86\,\Omega$ (after life cycle test). However, the change in resistance from EIS spectra reveals that higher charge transfer resulted in the superior capacitive performance of the full cell (AC//$KCo_{0.5}Ni_{0.5}PO_4$). The HSC-based AC//$KCo_{0.5}Ni_{0.5}PO_4$ full cell delivered a Coulombic efficiency of nearly ~96% (Figure 11e) with excellent stability, owing to a capacitance retention of 87.2% after 5000 cycles. The specific energy density (E) and specific power density (P)

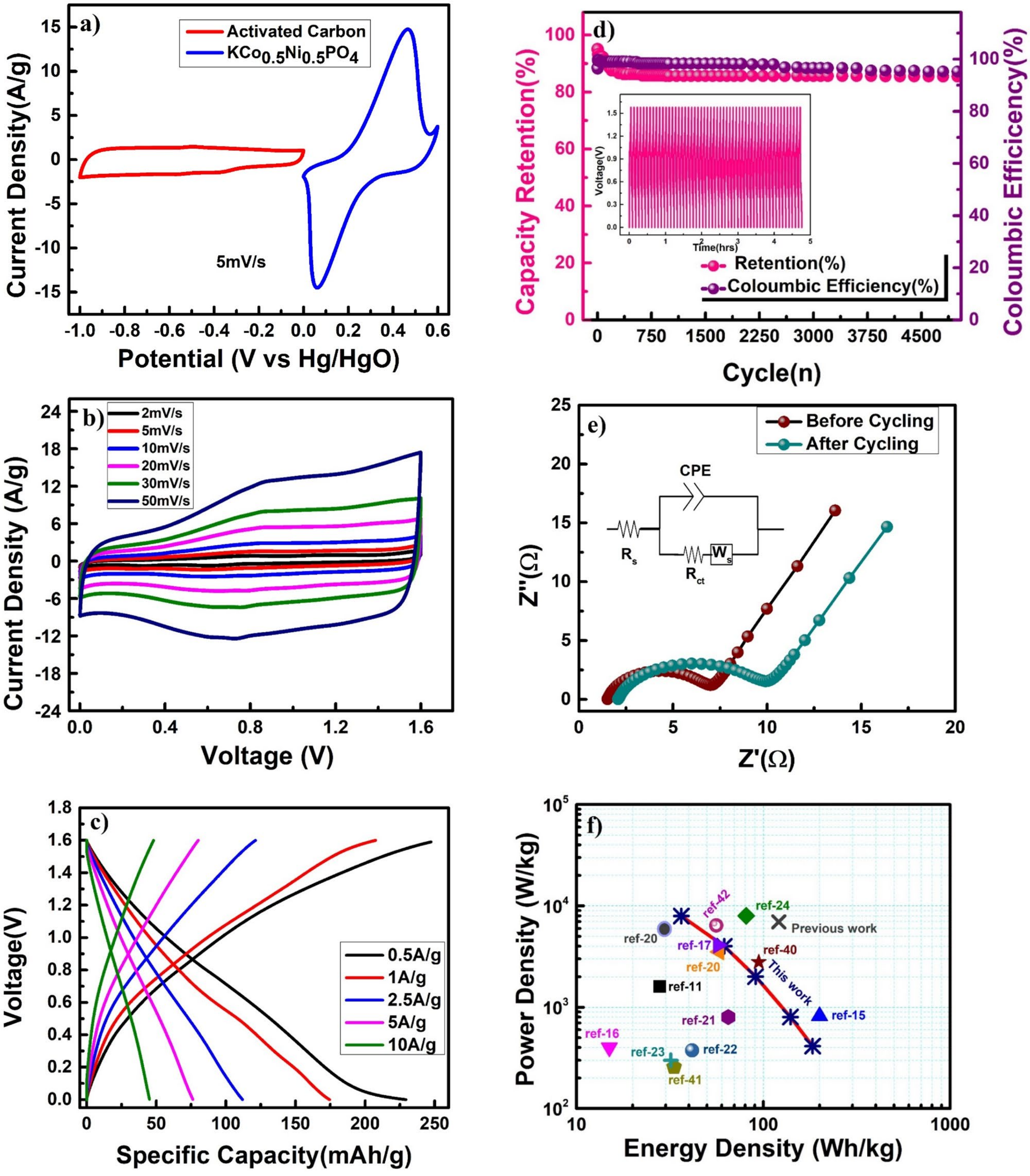

FIGURE 11 | (a) CV curves AC and KCoPO4 electrode at 5 mV/s in a three-electrode system, (b) CV curves of AC//$KCo_{0.5}Ni_{0.5}PO_4$ as HSCs in 2M KOH at different scan rates, (c) specific capacity of AC//$KCo_{0.5}Ni_{0.5}PO_4$ as HSCs in 2M KOH at different current densities, (d) capacitive retention and Coulombic efficiency of the HSCs device, (e) Nyquist at initial cycle and after 5000 cycles of the full cell in HSC mode, and (f) Ragone plot of AC//$KCo_{0.5}Ni_{0.5}PO_4$ as HSCs with another literature report.

of the HSCs can be calculated according to the equations presented below:

$$E(\mathrm{Wh/kg}) = \frac{1}{2}\frac{C_{\mathrm{HSCs}}}{3.6}V^2 \tag{15}$$

$$P(\mathrm{W/kg}) = \frac{E \times 3600}{t_{\mathrm{dis}}} \tag{16}$$

where C_{HSCs} is the specific capacitance, V is the potential window, and t_{dis} is the discharge time.

Figure 11f presents a Ragone plot of energy density vs. power capacity at different constant current densities. The full cell (AC//$KCo_{0.5}Ni_{0.5}PO_4$) delivered a maximum energy density equal to 183.7 Wh/kg at a 0.5 A/g current rate, achieving a power capacity close to 414 W/kg. The maximum power density equal to 7952 W/kg was obtained at an energy density of 36 Wh/kg at a current density of 10 A/g for the full cell. These enhanced full-cell performances in the two-electrode HSC mode of the $KCo_{0.5}Ni_{0.5}PO_4$ electrode validate the suitability of the new $KCo_{0.5}Ni_{0.5}PO_4$ electrodes for creating superior HSCs. In the HSC mode, we presented a comparison of the performance of alternative phosphate-based transition metal phosphate-containing electrodes in Table 1 [11, 15–18, 20–24, 40–42]. The table confirms the superior performance of the full cell in HSC mode, confirming the battery-type intercalating $KCo_{0.5}Ni_{0.5}PO_4$ electrode as a potential candidate to fabricate high-performing HSCs.

3 | Conclusions

$KCo_{1-x}Ni_xPO_4$ (x = 0, 0.1, 0.3, and 0.5) powder was synthesized through a facile two-step process utilizing a sol–gel auto-combustion method followed by calcination at elevated

TABLE 1 | Comparative study of electrochemical performances of cobalt and nickel-based phosphate electrode materials in full cells.

Electrode material (negative electrode//positive electrode)	Electrolyte	Specific capacitance	Energy density/ power density	Reference
AC//γ-$KCoPO_4$	1 M KOH	100 C/g at 0.6 mA/cm^2	ED = 28 Wh/kg at PD = 1600 W/kg	[11]
AC//$KNiPO_4$	2MKOH	168.5 mAh/g (capacitance: 935 F/g) at 1 A/g	ED = 200 Wh/kg PD = 819 W/kg	[15]
AC//$NaMn_{1/3}Ni_{1/3}Co_{1/3}PO_4$	2 M NaOH	45 F/g at 0.5 A/g	ED = 15 Wh/kg PD = 400 W/kg	[16]
AC//$Co_2P_2O_7$/MWCNT	1 M KOH	114 mAh/g at 2.9 A/g	ED = 57.3 Wh/kg at PD = 4100 W/kg	[17]
AC//$Co_3(PO_4)_2$	1 M NaOH	111.2 F/g at 5 mA/cm^2	ED = 29.20 Wh/kg at PD = 4687 W/kg	[18]
AC//$Co_3(PO_4)_2{\cdot}8H_2O$	1 M KOH	163 F/g at 2 mA/cm^2	ED = 58.12 Wh/kg at PW = 3520 W/kg	[19]
HPGC//$Ni_2P_2O_7$	1 M NaOH	183 F/g at 1 A/g	ED = 65 Wh/kg at PD = 800 W/kg	[20]
AC//$NH_4NiPO_4{\cdot}H_2O$	3 M KOH	1513 F/g at 5 A/g	ED = 41.6 Wh/ kg at PD = 375 W/kg	[21]
AC//$NaNiPO_4$	2 M NaOH	90 F/g at 0.3 A/g	ED = 32 Wh/kg at PD = 300 W/kg	[22]
AC//$KCo_{0.33}Ni_{0.67}PO_4{\cdot}H_2O$	1 M KOH	227 F/g at 1.5 A/g	ED = 80.64 Wh/kg at PW = 8000 W/kg	[23]
AC//$CoNiP_2O_7$/NF@PPy	2 M KOH	390 mAh/g at 2 A/g	ED = 94.6 Wh/kg at PD = 2791 W/kg	[40]
AC//$Ni_2P_2O_7$/$Co_2P_2O_7$	2 M KOH	2074 F/g at 5 A/g	ED = 33.3 Wh/kg at PD = 257 W/kg	[41]
AC//$Co_{0.125}Cu_{0.375}Mn_{0.5}(PO_4)_2$	1 M KOH	158.5 F/g @1 A/g	ED = 56 Wh/kg at PD = 6420 W/kg	[42]
AC//KCoPO4	2 M KOH	387 F/g at 1 A/g	ED = 121 Wh/kg at PD = 6947 W/kg	Previous work
AC//$KCo_{0.5}Ni_{0.5}PO_4$	2MKOH	173 mAh/g@0.5 A/g	ED = 183.5 Wh/kg at PD = 7952 W/kg	This work

temperatures of 600°C. Due to the synergistic interaction of Co^{2+} and Ni^{2+} ions in the phosphate framework, the incorporation of redox-mediated diffusive charge storage through the incorporation of Ni^{2+} on the Co^{2+} site resulted in a large-scale charge storage capacity coupled with capacitive-type surface charge storage on the $KCo_{1-x}Ni_xPO_4$ electrodes. The $KCo_{0.5}Ni_{0.5}PO_4$ electrodes delivered a specific capacity of 173 mAh/g (capacitance: 1038 F/g) at 0.5 A/g current density with excellent cyclic stability. Involvement of ~1:1 Co: Ni composition has a significant impact on charge storage in HSC mode. Intercalative (inner) and capacitive (outer) surface charge storage on the electrode were close to 58% and 42%, respectively, suggesting that the high capacitance of the electrode is due to the predominant intercalative pseudocapacitive charge storage behavior caused by the active involvement of $Co^{2+/3+}$ and $Ni^{2+/3+}$ redox couple-mediated charge storage. The superior cycle stability of $KCo_{0.5}Ni_{0.5}PO_4$ electrodes at 5 A/g for 5000 cycles, with 88.93% capacity retention and coulombic efficiency ($\eta = {}^{t_d}/_{t_c}$), was observed. In the potential window of 1.6 V in 2 M KOH electrolyte, the AC//$KCo_{0.5}Ni_{0.5}PO_4$ cell in HSC mode achieved the highest energy density, nearly 183.7 Wh/kg, with a power capacity of 414 W/kg. Moreover, the full cell (AC//$KCo_{0.5}Ni_{0.5}PO_4$) demonstrated an exceptionally high power capacity of about 7952 W/kg, which allowed it to store 36.4 Wh/kg of charge at a current rate of 10 A/g while maintaining excellent cycle stability. After 5000 cycles, AC//$KCo_{0.5}Ni_{0.5}PO_4$ HSCs coulombic efficiency has lost just 4.7%, demonstrating good capacity retention (87.2%) of its initial value. In conclusion, the $KCo_{0.5}Ni_{0.5}PO_4$ reported in this work showed promising application as an efficient, stable, and environmentally benign electrode for supercapacitors in grid-scale energy storage applications.

Acknowledgments

Krishna Gopal Nigam thanks the Department of Ceramic Engineering, IIT (BHU) Varanasi for its facility and support. The authors also thank Cellgrid Energy Pvt. Ltd. (Project no.: UID0991) for their financial support in completing this work. The author also thanks the Central Instrument Facility, IIT(BHU), for the characterization of the samples.

Conflicts of Interest

The authors declare no conflicts of interest.

Data Availability Statement

The data that support the findings of this study are available on request from the corresponding author. The data are not publicly available due to privacy or ethical restrictions.

References

1. R. Eisenberg, "Addressing the Challenge of Carbon-Free Energy," *ACS Energy Letters* 3, no. 7 (2018): 1521–1522, https://doi.org/10.1021/acsenergylett.8b00889.

2. S. Chu and A. Majumdar, "Opportunities and Challenges for a Sustainable Energy Future," *Nature* 488, no. 7411 (2012): 294–303, https://doi.org/10.1038/nature11475.

3. K. Subramanyan, M. L. Divya, and V. Aravindan, "Dual-Carbon Na-Ion Capacitors: Progress and Future Prospects," *Journal of Materials Chemistry A* 9, no. 15 (2021): 9431–9450, https://doi.org/10.1039/d0ta12099e.

4. E. Capacitors, "What Are Batteries, Fuel Cells, and Supercapacitors?," *Chemical Reviews* 104, no. 10 (2004): 4245–4270, https://doi.org/10.1021/cr020730k.

5. D. Kaufman, K. L. Hudson, and R. Mcclamrock, "Where Do Batteries End and Supercapacitors Begin?," *Science* 343 (2014): 1210–1212.

6. J. Liu, C. Xu, Z. Chen, S. Ni, and Z. X. Shen, "Progress in Aqueous Rechargeable Batteries," *Green Energy & Environment* 3, no. 1 (2018): 20–41, https://doi.org/10.1016/j.gee.2017.10.001.

7. J. Cherusseri, D. Pandey, and J. Thomas, "Symmetric, Asymmetric, and Battery-Type Supercapacitors Using Two-Dimensional Nanomaterials and Composites," *Batteries & Supercaps* 3, no. 9 (2020): 860–875, https://doi.org/10.1002/batt.201900230.

8. J. B. Goodenough and P. Singh, "Review-Solid Electrolytes in Rechargeable Electrochemical Cells," *Journal of the Electrochemical Society* 162, no. 14 (2015): A2387–A2392, https://doi.org/10.1149/2.0021514jes.

9. J. Ding, W. Hu, E. Paek, and D. Mitlin, "Review of Hybrid Ion Capacitors: From Aqueous to Lithium to Sodium," *Chemical Reviews* 118, no. 14 (2018): 6457–6498, https://doi.org/10.1021/acs.chemrev.8b00116.

10. G. Z. Chen, "Understanding Supercapacitors Based on Nano-Hybrid Materials With Interfacial Conjugation," *Progress in Natural Science: Materials International* 23, no. 3 (2013): 245–255, https://doi.org/10.1016/j.pnsc.2013.04.001.

11. N. Priyadharsini, S. Surendran, B. Senthilkumar, L. Vasylechko, and R. K. Selvan, "Synthesis and Electrochemical Performances of γ-KCoPO4 Nanocrystals as Promising Electrode for Aqueous Supercapatteries," *ChemElectroChem* 6, no. 2 (2019): 369–377, https://doi.org/10.1002/celc.201801440.

12. Y. Jiang, M. Hu, D. Zhang, et al., "Transition Metal Oxides for High Performance Sodium Ion Battery Anodes," *Nano Energy* 5 (2014): 60–66, https://doi.org/10.1016/j.nanoen.2014.02.002.

13. P. Singh, K. Shiva, H. Celio, and J. B. Goodenough, "Eldfellite, NaFe(SO4)2: An Intercalation Cathode Host for Low-Cost Na-Ion Batteries," *Energy & Environmental Science* 8, no. 10 (2015): 3000–3005, https://doi.org/10.1039/c5ee02274f.

14. L. Sharma and A. Manthiram, "Polyanionic Insertion Hosts for Aqueous Rechargeable Batteries," *Journal of Materials Chemistry A* 10, no. 12 (2022): 6376–6396, https://doi.org/10.1039/d1ta11080b.

15. M. Singh, S. Kumar, R. Mondal, P. Singh, R. Prakash, and N. Sharma, "Combustion-Synthesized KNiPO4: A Non-Toxic, Robust, Intercalating Battery-Type Pseudocapacitive Electrode for Hybrid Supercapacitors as a Large-Scale Energy Storage Solution," *Energy and Fuels* 37, no. 5 (2023): 4094–4105, https://doi.org/10.1021/acs.energyfuels.2c04092.

16. M. Minakshi, D. Meyrick, and D. Appadoo, "Maricite (NaMn1/3Ni1/3Co1/3PO4)/Activated Carbon: Hybrid Capacitor," *Energy and Fuels* 27, no. 6 (2013): 3516–3522, https://doi.org/10.1021/ef400333s.

17. A. Agarwal, S. Majumder, and B. R. Sankapal, "Carbon Nanotube-Functionalized Surface-Assisted Growth of Cobalt Phosphate Nanodots: A Highly Stable and Bendable all-Solid-State Symmetric Supercapacitor," *Energy and Fuels* 36, no. 11 (2022): 5953–5964, https://doi.org/10.1021/acs.energyfuels.2c00600.

18. H. Li, H. Yu, J. Zhai, L. Sun, H. Yang, and S. Xie, "Self-Assembled 3D Cobalt Phosphate Octahydrate Architecture for Supercapacitor Electrodes," *Materials Letters* 152 (2015): 25–28, https://doi.org/10.1016/j.matlet.2015.03.053.

19. P. K. Katkar, S. J. Marje, S. S. Pujari, S. A. Khalate, A. C. Lokhande, and U. M. Patil, "Enhanced Energy Density of all-Solid-State Asymmetric Supercapacitors Based on Morphologically Tuned Hydrous Cobalt Phosphate Electrode as Cathode Material," *ACS Sustainable Chemistry & Engineering* 7, no. 13 (2019): 11205–11218, https://doi.org/10.1021/acssuschemeng.9b00504.

20. B. Senthilkumar, Z. Khan, S. Park, K. Kim, H. Ko, and Y. Kim, "Highly Porous Graphitic Carbon and Ni2P2O7 for a High Performance Aqueous Hybrid Supercapacitor," *Journal of Materials Chemistry A* 3, no. 43 (2015): 21553–21561, https://doi.org/10.1039/c5ta04737d.

21. C. Chen, N. Zhang, X. Liu, et al., "Polypyrrole-Modified NH4NiPO4·H_2O Nanoplate Arrays on Ni Foam for Efficient Electrode in Electrochemical Capacitors," *ACS Sustainable Chemistry & Engineering* 4, no. 10 (2016): 5578–5584, https://doi.org/10.1021/acssuschemeng.6b01347.

22. M. Minakshi Sundaram and D. R. G. Mitchell, "Dispersion of Ni2+ Ions: Via Acetate Precursor in the Preparation of NaNiPO4 Nanoparticles: Effect of Acetate vs. Nitrate on the Capacitive Energy Storage Properties," *Dalton Transactions* 46, no. 40 (2017): 13704–13713, https://doi.org/10.1039/c7dt02444d.

23. B. Liang, Y. Chen, J. He, et al., "Controllable Fabrication and Tuned Electrochemical Performance of Potassium co-Ni Phosphate Microplates as Electrodes in Supercapacitors," *ACS Applied Materials & Interfaces* 10, no. 4 (2018): 3506–3514, https://doi.org/10.1021/acsami.7b14552.

24. X. Liu, W. Zang, C. Guan, et al., "Ni-Doped Cobalt-Cobalt Nitride Heterostructure Arrays for High-Power Supercapacitors," *ACS Energy Letters* 3, no. 10 (2018): 2462–2469, https://doi.org/10.1021/acsenergylett.8b01393.

25. M. Yang, N. Han, L. Shi, et al., "Effect of Nickel Doping on the Structure, Morphology and Oxygen Evolution Reaction Performance of cu-BTC Derived CuCoO2," *Dalton Transactions* 51, no. 22 (2022): 8757–8765, https://doi.org/10.1039/d2dt00970f.

26. Y. Liu, Z. Li, Y. You, X. Zheng, and J. Wen, "Synthesis of Different Structured FePO4 for the Enhanced Conversion of Methyl Cellulose to 5-Hydroxymethylfurfural," *RSC Advances* 7, no. 81 (2017): 51281–51289, https://doi.org/10.1039/c7ra09186a.

27. S. Vivekanandhan, M. Venkateswarlu, and N. Satyanarayana, "Ammonium Carboxylates Assisted Combustion Process for the Synthesis of Nanocrystalline LiCoO2 Powders," *Materials Chemistry and Physics* 109, no. 2–3 (2008): 241–248, https://doi.org/10.1016/j.matchemphys.2007.11.027.

28. Gangulibabu, D. Bhuvaneswari, N. Kalaiselvi, N. Jayaprakash, and P. Periasamy, "CAM Sol-Gel Synthesized LiMPO4 (M = Co, Ni) Cathodes for Rechargeable Lithium Batteries," *Journal of Sol-Gel Science and Technology* 49, no. 2 (2009): 137–144, https://doi.org/10.1007/s10971-008-1870-5.

29. N. K. Mishra, R. Mondal, T. Maiyalagan, and P. Singh, "Synthesis, Characterizations, and Electrochemical Performances of Highly Porous, Anhydrous Co0.5Ni0.5C2O4 for Pseudocapacitive Energy Storage Applications," *ACS Omega* 7, no. 2 (2022): 1975–1987, https://doi.org/10.1021/acsomega.1c05356.

30. C. Schlumberger and M. Thommes, "Characterization of Hierarchically Ordered Porous Materials by Physisorption and Mercury Porosimetry—A Tutorial Review," *Advanced Materials Interfaces* 8, no. 4 (2021): 1–25, https://doi.org/10.1002/admi.202002181.

31. J. Wen, J. Xie, H. Zhang, et al., "Constructing Multifunctional Metallic Ni Interface Layers in the g-C3N4 Nanosheets/Amorphous NiS Heterojunctions for Efficient Photocatalytic H2 Generation," *ACS Applied Materials & Interfaces* 9, no. 16 (2017): 14031–14042, https://doi.org/10.1021/acsami.7b02701.

32. A. Mukhtar, N. Mellon, S. Saqib, S. P. Lee, and M. A. Bustam, "Extension of BET Theory to CO2 Adsorption Isotherms for Ultra-Microporosity of Covalent Organic Polymers," *SN Applied Sciences* 2, no. 7 (2020): 1–4, https://doi.org/10.1007/s42452-020-2968-9.

33. G. Wang, Z. Yan, N. Wang, M. Xiang, and Z. Xu, "NiO/Ni Metal-Organic Framework Nanostructures for Asymmetric Supercapacitors," *ACS Applied Nano Materials* 4, no. 9 (2021): 9034–9043, https://doi.org/10.1021/acsanm.1c01628.

34. N. K. Mishra, A. K. Singh, R. Mondal, and P. Singh, "NiC2O4·2H2O Nanoflakes: A Novel Redox-Mediated Intercalative Pseudocapacitive Electrode for Supercapacitor Applications in Aqueous KOH and Neutral Na2SO4 Electrolytes," *ChemistrySelect* 7, no. 21 (2022): 1–13, https://doi.org/10.1002/slct.202201134.

35. N. K. Mishra, R. Mondal, and P. Singh, "Synthesis, Characterizations and Electrochemical Performances of Anhydrous CoC2O4 nanorods for Pseudocapacitive Energy Storage Applications," *RSC Advances* 11, no. 54 (2021): 33926–33937, https://doi.org/10.1039/d1ra05180f.

36. R. Sahoo, et al., "Redox-Driven Route for Widening Voltage Window in Asymmetric Supercapacitor," *ACS Nano* 12, no. 8 (2018): 8494–8505, https://doi.org/10.1021/acsnano.8b04040.

37. N. R. Chodankar, H. D. Pham, A. K. Nanjundan, et al., "True Meaning of Pseudocapacitors and Their Performance Metrics: Asymmetric Versus Hybrid Supercapacitors," *Small* 16, no. 37 (2020): 1–35, https://doi.org/10.1002/smll.202002806.

38. N. B. Velhal, J. Ahn, T. H. Yun, et al., "Exploring the Effect of Ultrafast Intensive Pulsed Light (IPL) Annealing on the Structure and Performance of Cobalt Oxide Electrodes for Supercapacitors," *ACS Applied Energy Materials* 6, no. 14 (2023): 7405–7418, https://doi.org/10.1021/acsaem.3c00656.

39. S. Rudra, S. das, P. K. Maji, et al., "Redox-Guided Synthesis of Au-V2O5-MnO2 Nanoflower Composites With Enhanced Electrical Conductance for Supercapacitor Applications," *ACS Applied Nano Materials* 6, no. 3 (2023): 1648–1659, https://doi.org/10.1021/acsanm.2c04584.

40. S. Sathishkumar, M. Karthik, R. Boopathiraja, et al., "Bimetal Pyrophosphate of CoNiP2O7@Polypyrrole Nanocomposite-Based Electrode for Hybrid Supercapacitor Applications," *Energy Technology* 12 (2024): 2301589, https://doi.org/10.1002/ente.202301589.

41. P. Matheswaran, P. Karuppiah, S. M. Chen, and P. Thangavelu, "A Binder-Free Ni2P2O7/Co2P2O7 nanograss Array as an Efficient Cathode for Supercapacitors," *New Journal of Chemistry* 44, no. 30 (2020): 13131–13140, https://doi.org/10.1039/d0nj00890g.

42. M. Z. Iqbal, et al., "Copper Doped Cobalt-Manganese Phosphate Ternary Composites for High-Performance Supercapattery Devices," *Journal of Energy Storage* 35, no. 2020 (2021): 102307, https://doi.org/10.1016/j.est.2021.102307.

Supporting Information

Additional supporting information can be found online in the Supporting Information section.